# Achieving ultra-high strength and ductility in Mg–9Al–1Zn–0.5Mn alloy via selective laser melting

Chang, Cheng; Liao, Hanlin; Yi, Lin; Dai, Yilong; Cox, Sophie C.; Yan, Ming; Liu, Min; Yan, Xingchen

*DOI:*
10.1016/j.apmate.2022.100097

Advanced Powder Materials 2 (2023) 100097

Contents lists available at ScienceDirect

Advanced Powder Materials

journal homepage: www.keaipublishing.com/en/journals/advanced-powder-materials

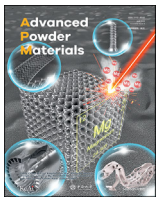

# Achieving ultra-high strength and ductility in Mg–9Al–1Zn–0.5Mn alloy via selective laser melting

Cheng Chang [a,c,d], Hanlin Liao [a,c], Lin Yi [a,b], Yilong Dai [b], Sophie C. Cox [d], Ming Yan [e,f], Min Liu [a,**], Xingchen Yan [a,*]

[a] Guangdong Provincial Key Laboratory of Modern Surface Engineering Technology, National Engineering Laboratory of Modern Materials Surface Engineering Technology, Institute of New Materials, Guangdong Academy of Sciences, Guangzhou 510651, China
[b] School of Materials Science and Engineering, Xiangtan University, Xiangtan 411105, China
[c] ICB UMR 6303, CNRS, Univ. Bourgogne Franche-Comté, UTBM, F-90010, Belfort, France
[d] School of Chemical Engineering, University of Birmingham, Edgbaston, Birmingham, B15 2TT, UK
[e] Department of Materials Science and Engineering, Southern University of Science and Technology, Shenzhen 518055, China
[f] Jiaxing Research Institute, Southern University of Science and Technology, Jiaxing 314050, China

ARTICLE INFO

*Keywords:*
Selective laser melting
Mg–Zn–Al–Mn alloy
Response surface analysis
Microstructural evolution
Mechanical properties

ABSTRACT

Fabrication of the Mg–9Al–1Zn–0.5Mn alloy with excellent mechanical performance using selective laser melting (SLM) technology is quite difficult owing to the poor weldability and low boiling point. To address these challenges and seek the optimal processing parameters, response surface methodology was systematically utilized to determine the appropriate SLM parameter combinations. Mg–9Al–1Zn–0.5Mn sample with high relative density (99.5 ± 0.28%) and favorable mechanical properties (microhardness = 95.6 ± 5.28 $HV_{0.1}$, UTS = 370.2 MPa, and $A_t$ = 10.4%) was achieved using optimized SLM parameters ($P$ = 120 W, $v$ = 500 mm/s, and $h$ = 45 μm). Sample is dominated by a random texture and microstructure is primarily constituted by quantities of fine equiaxed grains (α-Mg phase), a small amount of β-$Al_{12}Mg_{17}$ structures (4.96 vol%, including spherical: $[2\bar{1}\bar{1}0]_\alpha // [111]_\beta$ and long lath-like: $[2\bar{1}\bar{1}0]_\alpha // [1\bar{1}5]_\beta$ or $[\bar{1}011]_\alpha // [3\bar{2}\bar{1}]_\beta$), and some short rod-shaped $Al_8Mn_5$ nanoparticles. Benefiting from grain boundary strengthening, solid solution strengthening, and precipitation hardening of various nanoparticles (β-$Al_{12}Mg_{17}$ and $Al_8Mn_5$), high-performance Mg–9Al–1Zn–0.5Mn alloy biomedical implants can be fabricated. Precipitation hardening dominates the strengthening mechanism of the SLM Mg–9Al–1Zn–0.5Mn alloy.

## 1. Introduction

Magnesium (Mg) alloys have grasped considerable attention in the biomedical field owing to their excellent biological properties, ultra-low density close to the human bone, and no stress shielding phenomenon [1,2]. Although biodegradability of the Mg-based materials extensively promotes their applications in the biological fields, nonetheless, the mechanical properties of Mg alloys will be significantly reduced after the *in-vivo* degradation, resulting in a premature fracture of the implants [3]. Hence, designing and fabricating a type of high-performance Mg-based materials possessing good strength and toughness has become one of the current important chanllenges.

Mg–Al–Zn–Mn alloy series is one of the most popular compositions among cast magnesium family. Al acts as a reinforcing element, increasing strength and fluidity for casting, while Zn and Mn enhance biocompatibility, plasticity, and corrosion resistance [4,5]. Thus, Mg–Al–Zn–Mn alloy, in particular to Mg–9Al–1Zn–0.5Mn alloy, has emerged as a promising candidate for bone implants since it combines suitable mechanical properties and corrosion resistance [6]. Nevertheless, restricted by the inherent nature of the hexagonal close-packed (HCP) structure (i.e., only a few slip systems in α-Mg matrix), it is not possible to fabricate the Mg alloy at low or room temperatures (i.e., below 225 °C) [7,8]. As such, forming Mg–9Al–1Zn–0.5Mn alloy only can be conducted at elevated temperature. Mg–9Al–1Zn–0.5Mn alloy manufactured via equilibrium solidification (i.e., casting) always have quite a large grain size, leading to poor mechanical properties (i.e., ultimate tensile strength≤250 MPa, elongation≤5%) [9]. While other thermoforming techniques (i.e., extrusion and rolling) often result in a

* Corresponding author.
** Corresponding author.
*E-mail addresses:* liumin@gdas.gd.cn (M. Liu), yanxingchen@gdinm.com (X. Yan).

https://doi.org/10.1016/j.apmate.2022.100097
Received 7 September 2022; Received in revised form 19 October 2022; Accepted 23 October 2022
Available online 31 October 2022

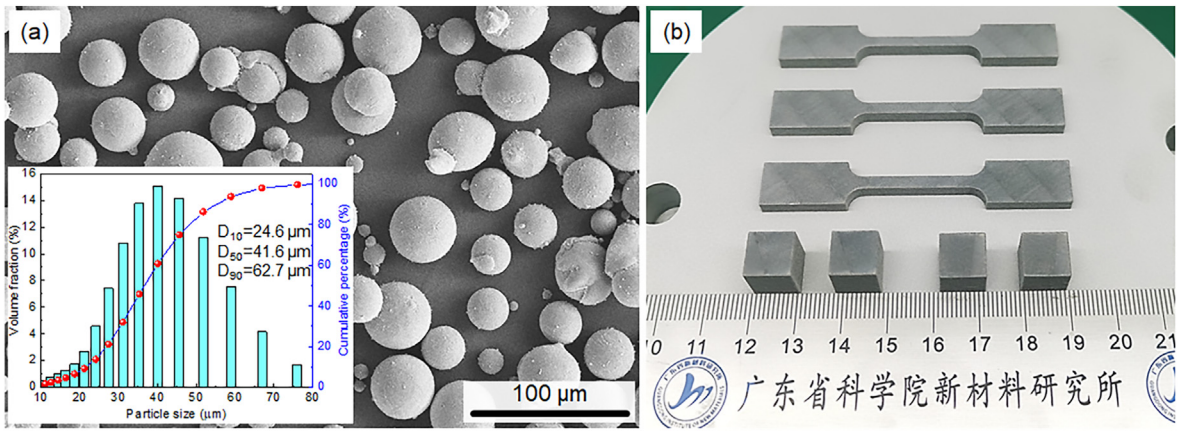


**Fig. 1.** (a) Powder morphology with an inset of particle size distribution; (b) typical SLM Mg–9Al–1Zn–0.5Mn samples.

typical basal texture within the α-Mg matrix due to the characteristics of the processing methods [10]. The anisotropy of the microstructure will greatly impair the mechanical properties of the Mg–9Al–1Zn–0.5Mn alloy. Notably, manufacturing bone implant is extremely difficult via these thermoforming approaches since designs often exhibit internal structures, curved surfaces, and ultra-fine lattices. A series of post-heat treatments and machining processes are needed to meet the requirements of the bone implants. Hence, new manufacturing methods are in great demands to obtain intricate structures using these Mg alloys.

Selective laser melting (SLM), an attractive metal additive manufacturing techniques, can directly manufacture high-density metallic parts without any molds [11,12]. A 'point-by-point, track-by-track, layer-by-layer' method to selectively fuse the metallic powder bed using one or multiple laser beams endows it a high flexibility to fabricate complex structures. Benefit from its high-energy input ($10–10^3$ J/mm$^3$ [13,14]) and ultra-high cooling rate ($10^4–10^6$ K/s [15,16]), tailored microstructure and tunable sophisticated structures can be obtained jointly from micro-scale to macro-scale. Moreover, advantages like reusable recycled powders, high manufacturing precision, little or no post-machining also broaden the possibilities of the SLM-fabricated Mg alloy products. Thus, different types of Mg-based materials have been fabricated via SLM process, including pure Mg [17], Mg–Zn alloy [10], Mg–Zn–Ca alloys [18,19], Mg–Zn–Zr alloys [20], Mg–Al–Zn alloys [21], and rare-earth containing Mg alloys [22].

However, many challenges still exist to manufacture Mg alloys via SLM: (I) poor weldability due to a low boiling point (~1091 °C) and excellent affinity for oxygen; (II) easily producing hot cracks owing to a large coefficient of thermal expansion ($\alpha = 27.6 \pm 0.6 \times 10^{-6}$/K at 380 °C for Mg–1Al alloy [23]); (III) readily producing micro-pores caused by the hydrogen escape and high vaporization pressure phenomena. As known, rare earth (Re) elements like La, Ce, Y, Nd, Gd, and Sm, etc., have the functions of removing H, O, Fe and other inclusions in the melted Mg alloys, purifying the SLM-fabricated products. Nevertheless, some Re elements would be accumulated in the human organs, in particular to the spleen, liver, lung, and kidney, along with the degradation of the Mg–Re alloys [24]. Hence, to ensure biosafety, exploring high-performance SLM Mg alloys without Re elements, like Mg–Al–Zn–Mn alloys, attracts much attention.

So far, restricted by the multiple limitations of Mg alloy itself and the difficulty of powder acquisition, there are relatively few reports on the SLM-produced Mg–Al–Zn–Mn alloys. Most obtained Mg–xAl powders with different compositions via mechanical ball milling method and manufactured the corresponding SLM samples [25,26]. Apparently, lots of unfused Al particles were segregated within the SLM samples, leading to a significant reduction of their mechanical properties [6]. A few researchers used pre-alloyed Mg–9Al–1Zn powder to study the effects of the SLM processing parameters on the microstructure and mechanical properties of the SLM-produced samples [5]. Nonetheless, they only focused on the scanning velocity and hatch distance, while ignoring the influence of the laser power on the material properties, let alone the mechanism of the different factors on the target performances. Moreover, even though the addition of nanoparticles is an effective route to boost their ultimate tensile strength (~345 MPa), a significant reduction in elongation (~1.1%) will severely limit their applications in implants [27].

**Table 1**
Chemical composition of the Mg–9Al–1Zn–0.5Mn powder and the samples fabricated using different manufacturing methods (wt.%).

| Elements | Al | Zn | Mn | Fe | Si | Cu | Mg |
|---|---|---|---|---|---|---|---|
| Powder | 8.69 | 0.63 | 0.23 | 0.0021 | 0.038 | 0.003 | Bal. |
| Cast state | 8.3 | 0.35 | 0.50 | 0.005 | 0.1 | 0.03 | Bal. |
| SLM state | 9.53 | 0.59 | 0.28 | 0.0025 | 0.04 | 0.003 | Bal. |

To systematically study the effects of the SLM processing parameters, especially the interaction factors, on the microstructure and mechanical properties of the SLM Mg–9Al–1Zn–0.5Mn alloy, a series of central composite design (CCD) experiments were conducted and analyzed in this research. Solidification process, microstructural evolution, and strengthening mechanism were studied in detail to fill the research gap within the SLM community and offer a theoretical guide to manufacture a high-property SLM Mg–9Al–1Zn–0.5Mn alloy for biomedical applications.

## 2. Experimental details

### 2.1. Raw material and SLM process

As displayed in Fig. 1, spherical gas-atomized Mg–9Al–1Zn–0.5Mn powder were supplied by Institute of New Materials, Guangdong Academy of Sciences, and the particle size distribution ($D_{10}$ = 24.6 μm, $D_{50}$ = 41.6 μm and $D_{90}$ = 62.7 μm) was detected using a laser diffraction powder analyzer (Mastersizer 2000, UK). The cast Mg–9Al–1Zn–0.5Mn alloy ingots were purchased from Dongguan Eontec. Co. Ltd., China.

To determine the composition changes before and after SLM fabrication, chemical compositions of the powders and samples under different states were characterized via an ICP-OES (SPECTROGREEEN, Spectro Analytical Instruments GmbH, Germany), respectively. The corresponding reults are listed in Table 1.

To reduce the possibility of oxidation or even explosion of Mg-based alloy powders during the SLM process, a home-made SLM system (GDINM-D150) for fabricating Mg-based alloys was developed, as exhibited in Fig. 2. An explosion-proof filter system was specially customized to store the recycled Mg-based powders (i.e., ① in Fig. 2). To

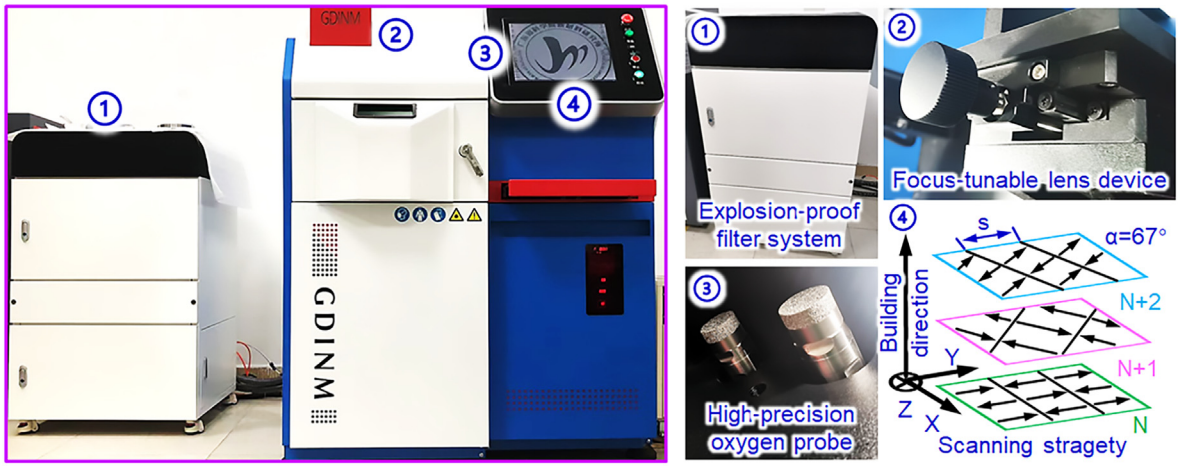


**Fig. 2.** Self-developed SLM system (GDINM-D150) alongside with featured devices.

**Table 2**
SLM parameters adopted in this study.

| Laser parameters | Value/Unit |
|---|---|
| Wavelength ($\lambda$) | |
| Rotation angle ($\alpha$) | 67° |
| Spot size ($d$) | 45 ± 4 μm |
| Stripe width ($s$) | 5 mm |
| Layer thickness ($t$) | 40 μm |
| Preheat temperature ($T$) | 120 °C |
| Hatch distance ($h$) | Low level (−1) = 40 μm; High level (+1) = 50 μm |
| Laser power ($P$) | Low level (−1) = 60 W; High level (+1) = 150 W |
| Scanning velocity ($v$) | Low level (−1) = 400 mm/s; High level (+1) = 600 mm/s |

**Table 3**
Face-centered CCD matrix adopted in this study and the corresponding results.

| No. | Independent variable | | | Dependent variables (responses) | |
|---|---|---|---|---|---|
| | P (W) | v (mm/s) | h (μm) | Average relative density (%) | Average microhardness ($HV_{0.1}$) |
| 1 | 105 | 500 | 40 | 99.6 ± 0.21 | 92.8 ± 2.56 |
| 2 | 105 | 500 | 45 | 99.7 ± 0.15 | 94.5 ± 3.77 |
| 3 | 60 | 500 | 45 | 81.9 ± 0.96 | 83.8 ± 5.12 |
| 4 | 60 | 600 | 40 | 74.8 ± 0.81 | 75.2 ± 2.18 |
| 5 | 105 | 500 | 45 | 98.7 ± 0.88 | 93.2 ± 1.34 |
| 6 | 105 | 600 | 45 | 96.6 ± 0.91 | 90.4 ± 5.11 |
| 7 | 105 | 500 | 45 | 98.3 ± 0.67 | 92.8 ± 3.24 |
| 8 | 60 | 400 | 50 | 80.9 ± 0.86 | 82.6 ± 4.58 |
| 9 | 105 | 500 | 50 | 95.9 ± 0.95 | 92.3 ± 6.51 |
| 10 | 105 | 500 | 45 | 97.2 ± 0.53 | 93.1 ± 2.24 |
| 11 | 150 | 400 | 50 | 96.2 ± 0.48 | 92.0 ± 2.67 |
| 12 | 105 | 500 | 45 | 97.7 ± 0.26 | 93.6 ± 5.13 |
| 13 | 60 | 600 | 50 | 71.8 ± 0.93 | 73.8 ± 4.27 |
| 14 | 150 | 400 | 40 | 98.3 ± 0.44 | 94.4 ± 3.18 |
| 15 | 150 | 600 | 50 | 97.7 ± 0.68 | 93.6 ± 6.25 |
| 16 | 105 | 400 | 45 | 98.3 ± 0.95 | 93.4 ± 4.11 |
| 17 | 105 | 500 | 45 | 99.5 ± 0.21 | 93.7 ± 5.04 |
| 18 | 150 | 500 | 45 | 99.4 ± 0.33 | 96.1 ± 3.27 |
| 19 | 150 | 600 | 40 | 97.2 ± 0.98 | 93.6 ± 4.28 |
| 20 | 60 | 400 | 40 | 87.6 ± 0.84 | 85.5 ± 2.18 |

alleviate keyhole-induced micro-pores during the SLM fabrication, a focus-tunable lens device was mounted near the galvo mirror so as to slightly adjust the laser focal length (i.e., ② in Fig. 2). Besides, two high-precision oxygen probes (i.e., ③ in Fig. 2, detection accuracy = ±3 ppm) were quipped in the working chamber to detect the oxygen content. Multiple scanning strategies, especially an alternating X/Y raster strategy with a rotation angle of 67° were chosen (i.e., ④ in Fig. 2). SLM-produced cubic samples for material characterization (10 mm × 10 mm × 10 mm) and dog bone specimens for tensile testing (73 mm × 11 mm × 3.5 mm) were manufactured in (Fig. 1b). To avoid the oxidation in the SLM process, oxygen content in the working chamber was set to below 30 ppm via pumping a high-purity argon flow (99.999 vol%).

In this study, central composite face-centered design (CCF), a second order experimental design with a full factorial, was selected to code the independent variables and establish the experiment matrix via a Minitab Statistical Software. Ranges of the explored SLM parameters are listed in Table 2. Experiment matrix including independent variables (laser power, scanning velocity, and hatch distance) and dependent variables (average relative density and average microhardness) are summarized in Table 3 after a series of explorations. Then, response surface methodology (RSM) was conducted for optimizing the SLM parameters and a regression equation was calculated to predict the aforementioned responses. A second order polynomial regression equation as exhibited in Eq. (1) is used to predict the response by considering the input parameters [28]:

$$y = a_0 + \sum_{i=1}^{k} a_i x_i + \sum_{i=1}^{k} a_{ii} x_i^2 + \sum_{i,j=1,j\neq i}^{k} a_{ij} x_i x_j \quad (1)$$

where $y$ is response, $a_0$ is average of responses, $a_i$, $a_{ii}$, and $a_{ij}$ are response coefficients. The 2nd, 3rd, and 4th terms denote the main, quadratic, and interaction effects, respectively.

### 2.2. Material characterization and mechanical properties

An optical microscope (OM, Leica Dmi5000 m, Germany) and a field emission scanning electron microscope (FE-SEM, ZEISS GeminiSEM 300, Germany) equipped with an energy-dispersive x-ray spectroscopy (EDS, EDAX XLT TEM-SDD, America) were used to study the microstructure of the Mg alloy samples. Each specimen was carefully polished using SiC grinding papers and etched for 15 s in a mixed solvent of nitric acid and ethanol (4 ml nitric acid and 96 ml ethanol). The phase composition was detected by x-ray diffraction (XRD) using a RIGAKU Smartlab XRD equipped with 9 kW X-ray emitter at 40 kV and 100 mA in a 2θ range of 30–90° with a scanning step size of 0.02° and scanning speed of 6 s per step. Crystallographic orientations were characterized via an electron back-scattering diffraction (EBSD) spectrometer (Oxford Ultim max 65, UK) and analyzed using the Channel 5 software. Grain size distribution was obtained as per the ISO 13067:2020 standard. A transmission electron microscope (JEOL JEM-2100F, Japan) was used to study the nanostructures and the distribution of precipitates. To reveal the distribution of nanoprecipitates in different micro-regions, high-angle annular dark-field scanning transmission electron microscopy (HAADF-STEM) with EDS analysis was also performed.

Relative densities of the SLM Mg–9Al–1Zn–0.5Mn alloys samples

**Table 4**
ANOVA results for the relative density.

| Source | Degrees of freedom | Adj. SS | Adj. MS | F-value | P-value |
|---|---|---|---|---|---|
| Model | 5 | 1028.80 | 205.761 | 106.08 | 0.000 |
| P | 1 | 618.33 | 618.331 | 318.78 | 0.000 |
| v | 1 | 23.09 | 23.088 | 11.9 | 0.004 |
| h | 1 | 15.91 | 15.906 | 8.2 | 0.013 |
| $P^2$ | 1 | 346.7 | 346.698 | 178.74 | 0.000 |
| Pv | 1 | 24.78 | 24.782 | 12.78 | 0.003 |
| Error | 14 | 27.16 | 1.940 | | 0.000 |
| Lack-of-Fit | 9 | 20.28 | 2.253 | 1.64 | 0.305 |
| Pure error | 5 | 6.88 | 1.375 | | |
| Total | 19 | 1055.96 | | | |

*$R^2 = 0.9743$, Adj. $R^2 = 0.9651$, Pred. $R^2 = 0.9353$.

**Table 5**
ANOVA results for the microhardness.

| Source | Degrees of freedom | Adj. SS | Adj. MS | F-value | P-value |
|---|---|---|---|---|---|
| Model | 7 | 583.828 | 83.404 | 191.00 | 0.000 |
| P | 1 | 382.405 | 382.405 | 875.74 | 0.000 |
| v | 1 | 24.628 | 24.628 | 56.40 | 0.000 |
| h | 1 | 4.032 | 4.032 | 9.23 | 0.010 |
| $P^2$ | 1 | 29.126 | 29.126 | 66.70 | 0.000 |
| $v^2$ | 1 | 9.288 | 9.288 | 21.27 | 0.001 |
| $h^2$ | 1 | 3.773 | 3.773 | 8.64 | 0.012 |
| Pv | 1 | 24.383 | 24.383 | 55.84 | 0.000 |
| Error | 12 | 5.240 | 0.437 | | |
| Lack-of-Fit | 7 | 2.952 | 0.422 | 0.92 | 0.556 |
| Pure Error | 5 | 2.288 | 0.458 | | |
| Total | 19 | 589.068 | | | |

*$R^2 = 0.9911$, Adj. $R^2 = 0.9859$, Pred. $R^2 = 0.9716$.

were measured based on the Archimedes principle via a Mettler-Toledo ME-TE analytical balance. A theoretical density value of the SLM Mg–9Al–1Zn–0.5Mn alloy used in this study is 1.82 g/cm$^3$. Microhardness of the samples was measured using a Vickers hardness tester (EmcoTest Dura Scan 70G5, Austria) with a load of 100 gf and an indentation time of 20 s. Ten indentations were randomly conducted on the polished surface and the average microhardness value was calculated. Tensile tests were carried out at room temperature according to the ASTM E8 M at a displacement rate of 0.5 mm/min. Mechanical properties including ultimate tensile strength (UTS), yield strength (YS), and fracture strain were recorded directly from a Zwick/Roell Z100 tensile tester. The value of the strain-to-failure was read through the strain gauge and electronic extensometer with a range of 10 mm that were equipped on the gauge section of the test samples. Then, a percentage total elongation at fracture ($A_t$) and elastic modulus ($E$) were measured and calculated on the basis of the ASTM E111-17 standard. The fracture surfaces of the tensile samples were inspected using SEM.

## 3. Results and discussions

### 3.1. Analysis of variance (ANOVA)

To seek the appropriate SLM parameter combinations, relative density (RD, %) and microhardness (HV, $HV_{0.1}$) were selected as the principal optimization objectives. A series of experiments based on the CCF design and corresponding results were conducted and summarized in Table 3. After using the RSM analysis, ANOVA results of the responses were listed in Table 4 and Table 5, respectively.

As displayed in Table 4, F-value of this model is 106.08, indicating a significant model. Specifically, P-value of each model term also existed at an ultra-low level ($0.000 \ll \alpha = 0.05$), illustrating the selected linear (i.e., $P$, $v$, $h$), square (i.e., $P^2$), and interactive terms (i.e., $Pv$) are quite significant. Thus, prediction model between relative density (RD, %) and these main processing parameters can be determined as below (eq. (2)):

$$RD^4 = 15215560.2 + 2705095.304P - 180724.891v - 809570.4708h - 13199.65811P^2 + 1255.123133Pv \quad (2)$$

High $R^2$ (i.e., 0.9743) and predicted $R^2$ (i.e., 0.9353) also demonstrate that this mathematical model can predict the response for new observations well.

Similarly, as for the microhardness response, F-value of the model is 191.00 with a low P-value ($0.000 \ll \alpha = 0.05$), indicating high confidence of this one (Table 5). Moreover, P-values of model terms are much low ($\ll 0.05$), highlighting the chosen linear (i.e., $P$, $v$, $h$), square (i.e., $P^2$, $v^2$, $h^2$), and interactive terms (i.e., $Pv$) are quite significant. Therefore, mathematical model between microhardness (HV, $HV_{0.1}$) and these main processing parameters were confirmed (eq. (3)):

$$HV^4 = -325937463.4 + 813106.8716P + 368778.2679v + 11839113.94h - 4651.700757P^2 - 532.6153947v^2 - 135759.0327h^2 + 1123.123767Pv \quad (3)$$

High $R^2$ (i.e., 0.9911) and adj. $R^2$ (i.e., 0.9859) display this model well fit the experimental data.

To obtain the SLM parameter combinations with high density and microhardness, a response optimizer was applied to further seek processing parameters and the predicted values thereof. RD is a vital factor affecting the microstructure and mechanical properties of the SLM samples. Hence, RD was set to 100%, and the microhardness was expected to be as high as possible. As presented in Fig. 3, when a series of

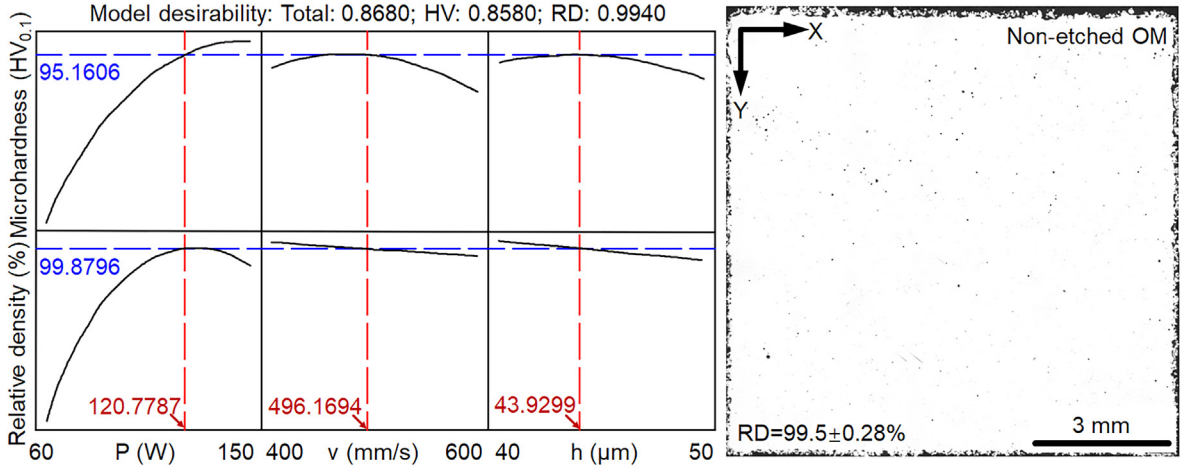


**Fig. 3.** Response optimizer results of microhardness and RD with a non-etched OM inset taken from the typical SLM samples fabricated using optimized parameters.

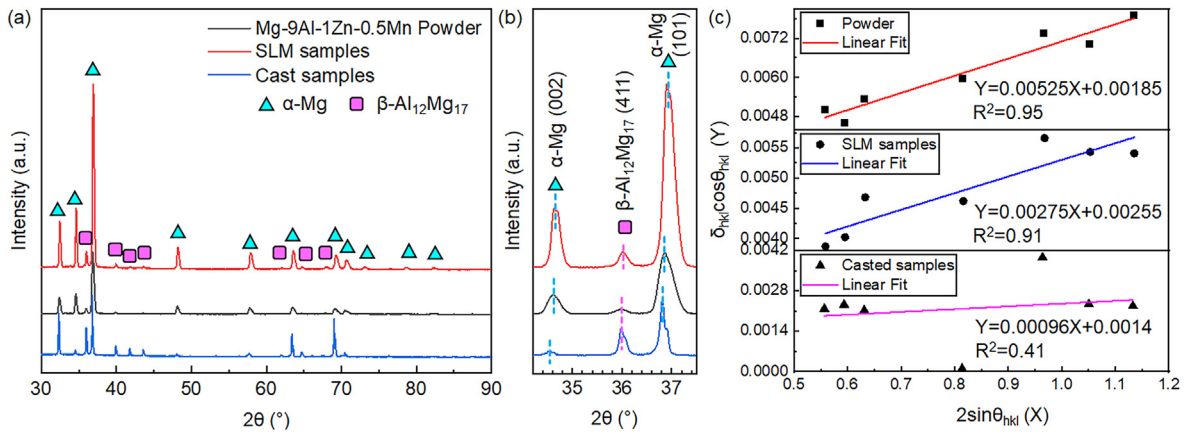


**Fig. 4.** Phase composition and the average effective micro strain of the different Mg–9Al–1Zn–0.5Mn states: (a) XRD curves; (b) magnified view of (a); (c) $\delta_{hkl}\cos\theta_{hkl}$ (Y)-$2\sin\theta_{hkl}$ (X) curves.

**Table 6**
Phase volumetric fraction and average dislocation density in the different Mg–9Al–1Zn–0.5Mn states.

| | Phase fraction (vol%) | | Key indicators calculated using W–H method | | |
|---|---|---|---|---|---|
| | α-Mg | β-$Al_{12}Mg_{17}$ | $D$ (nm) | $\epsilon$ | $\rho_d$ ( × $10^{14}$ $m^{-2}$) |
| Powder | 94.96 | 5.04 | 83.27 | 0.00525 | 7.40 |
| SLM state | 95.04 | 4.96 | 60.41 | 0.00275 | 5.35 |
| Cast state | 72.80 | 27.20 | 110.04 | 0.00096 | N/A |

processing parameters (i.e., $P = 120.7787$ W, $v = 496.4694$ mm/s and $h = 43.9299$ μm) was locked in accordance with the above two models, theoretical RD (99.8796%) and microhardness (95.1606 $HV_{0.1}$) can be determined. Then, to verify the accuracy of the established models, cubic samples were further fabricated using the processing parameter combinations (i.e., $P = 120$ W, $v = 500$ mm/s and $h = 45$ μm) based on the equipment conditions and Table 2. After measuring and calculating, RD and microhardness of the SLM samples are 99.5 ± 0.28% (Figs. 3) and 95.6 ± 5.28 $HV_{0.1}$, proving the accuracy and validity of the prediction model. Hence, SLM parameters (i.e., $P = 120$ W, $v = 500$ mm/s and $h = 45$ μm) was chosen as the optimized combinations to manufacture more SLM samples for latter microstructure observations and mechanical property tests.

### 3.2. Phase composition

Two main phases, α-Mg phase (JCPDS # 35–0821) and β-$Al_{12}Mg_{17}$ phase (JCPDS # 73–1148), were detected in the XRD spectra (Fig. 4a). As displayed in Fig. 4b, there is little difference in the peak positions of the cast, powder and the SLM states, indicating a low level residual stress within the SLM samples. Thus, the high-temperature preheat treatment (i.e., 120 °C) applied in the SLM process has an excellent effect on the removal of residual stress, thereby avoiding the possibility of the residual stress induced cracks. Interestingly, as depicted in Fig. 4b, relative intensity of β-$Al_{12}Mg_{17}$ phase within the powder and SLM samples is noticeably lower than the cast equivalent. To quantitatively compare the phase contents within the different Mg–9Al–1Zn–0.5Mn samples, the Reference Intensity Ratio (RIR) and Rietveld Refinement methods [29,30] was utilized to calculate the volume fraction of the different phases. As listed in Table 6, content of the β-$Al_{12}Mg_{17}$ phase in the cast state (27.20 vol%) is much higher than that of the powder (5.04 vol%) and SLM samples (4.96 vol%). It can be ascribed to the ultra-high cooling rate of the vacuum atomization ($10^3$–$10^5$ K/s [31]) and SLM process ($10^4$–$10^6$ K/s [15]), leading to a short existence of the Mg alloy melt. Hence, there is not enough time for the β-$Al_{12}Mg_{17}$ phase to form and grow.

To further analyze the dislocation density triggered by the rapid cooling rate, Williamson-Hall (W–H) plot method [32] was utilized to calculate the dislocation density within the different Mg–9Al–1Zn–0.5Mn states:

$$\delta_{hkl} \bullet \cos\theta_{hkl} = \frac{\lambda}{D} + 2\epsilon \bullet \sin\theta_{hkl} \quad (4)$$

where $\delta_{hkl}$ is the full width at half maximum intensity (FWHM) of the different states, $\theta_{hkl}$ is the Bragg refraction angle, $D$ is the average subgrain size, $\lambda$ is the wavelength of the x-ray (for Cu radiation, $\lambda = 0.15405$ nm), $\epsilon$ is the average effective microstrain.

Thus, average subgrain size ($D$, nm) and average effective microstrain ($\epsilon$) of the different Mg–9Al–1Zn–0.5Mn states can be obtained from the $\delta_{hkl}\cos\theta_{hkl}$ (Y) vs. $2\sin\theta_{hkl}$ (X) linear functions (Fig. 4a). The diffraction profiles used for this part were the (100), (002), (101), (102), (110), (103), and (200) crystal planes of the α-Mg phase. Then, the dislocation density ($\rho_d$, $m^{-2}$) is calculated from the following equation [33,34]:

$$\rho_d = \frac{2\sqrt{3}\epsilon}{bD} \quad (5)$$

Where $b$ is the Burgers vector ($b = 0.295$ nm) [33]. Key indicators calculated using W–H method and the dislocation density within the different states are listed in Table 6 and plotted in Fig. 4c.9.

As displayed in Fig. 4c and Table 6, extremely high cooling rate results in an ultra-low subgrain size and a great microstrain within the powder (i.e., $D = 83.27$ nm and $\epsilon = 0.00525$) and the SLM samples (i.e., $D = 60.41$ nm and $\epsilon = 0.00275$) compared to the cast alloy (i.e., $D = 110.04$ nm and $\epsilon = 0.00096$). Therefore, the dislocation densities in the powder and SLM samples can separately reach $7.40 \times 10^{14}$ $m^{-2}$ and $5.35 \times 10^{14}$ $m^{-2}$, which will further promote their microhardness and strength. Notably, subgrain size obtained from the cast samples exceeds 100 nm and the Coefficient of Determination (i.e., $R^2$) of the linear fit is only 0.41, indicating that the W–H method is not suitable for analyzing the cast samples with large subgrain (>100 nm). Besides, the microstrain in the as-cast state is only 0.00096, illustrating an ultra-low dislocation density level within the cast specimens.

### 3.3. Microstructural evolution

Fig. 5 presents the microstructure of the cast samples. Typical primary α-Mg dendrites with secondary arms are clearly detected in Fig .5a. A dendritic segregation containing a large amount of coarse and lamellar β-$Al_{12}Mg_{17}$ phase along the grain boundaries of the α-Mg dendrites can be observed in Fig. 5b and c. Based on the solidification theory and the Mg–Al phase diagram, the divorced eutectic α-Mg and continuous

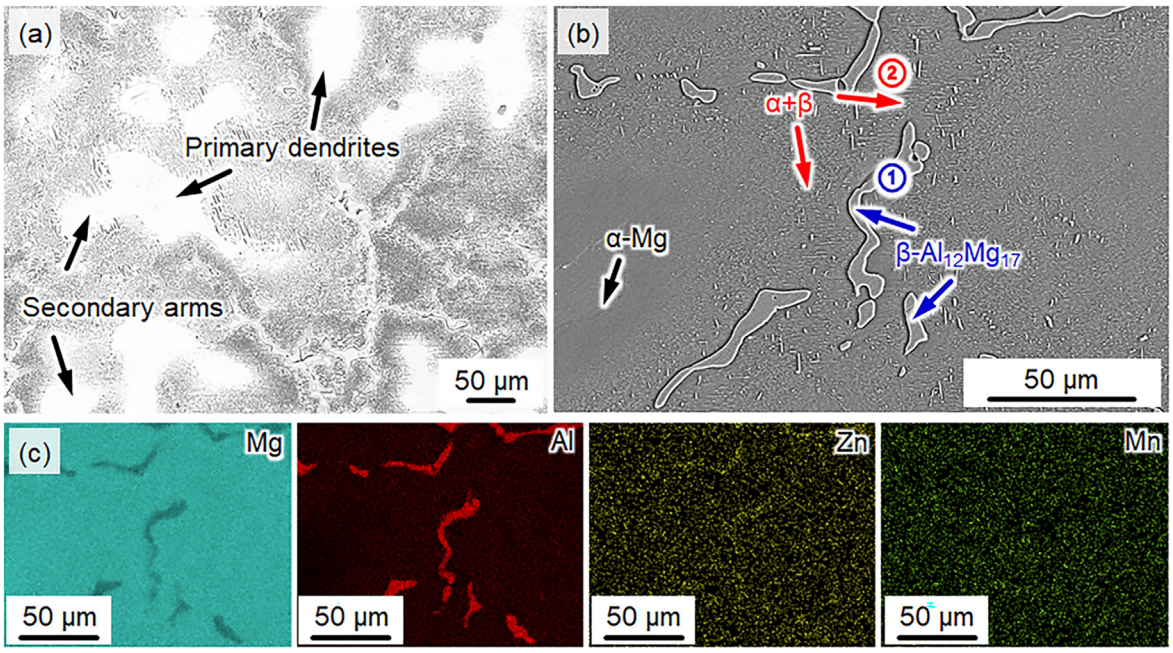


**Fig. 5.** Microstructure of the cast Mg–9Al–1Zn–0.5Mn samples: (a) OM; (b) SEM; (c) main elements distribution analyzed by EDS.

**Table 7**
EDS analyzing results of the different micro-regions of the cast samples.

| Terms | Region 1 | | Region 2 | |
|---|---|---|---|---|
| | Weight (wt.%) | Atom (at.%) | Weight (wt.%) | Atom (at.%) |
| Mg | 65.40 | 68.92 | 76.64 | 79.75 |
| Al | 31.40 | 29.82 | 20.33 | 19.06 |
| Zn | 3.06 | 1.20 | 2.82 | 1.09 |
| Mn | 0.14 | 0.06 | 0.21 | 0.10 |

β-$Al_{12}Mg_{17}$ simultaneously formed on the primary α-Mg, and then the secondary β-$Al_{12}Mg_{17}$ lamellar structures discontinuously precipitated from the supersaturated α-Mg matrix. Furthermore, reticular β-$Al_{12}Mg_{17}$ (micro-region 1) and α-Mg + needle-like β-$Al_{12}Mg_{17}$ structures (micro-region 2) can be observed in Fig. 5b. Thus, according to the EDS results of the different micro-regions (Table 7), three typical microstructures can be determined: primary α-Mg (black arrows), divorced eutectic α-Mg+β-$Al_{12}Mg_{17}$ (red arrows) and reticular β-$Al_{12}Mg_{17}$ (blue arrows).

Fig. 6 shows the microstructure features of the SLM Mg–9Al–1Zn–0.5Mn samples. Laser tracks (pink arrows) and molten pools (red arrows) can be clearly detected as displayed in Fig. 6a and d. A large quantity of equiaxed grains were formed within the center of the molten pools, as marked by black arrow in Fig. 6d; while only a small number of columnar dendrites were generated at the boundaries of the molten pools (blue arrow in Fig. 6d). Interestingly, a few irregular micropores (purple arrow) also formed at these boundaries as detected in Fig. 6d. It can be mainly ascribed to the lack of fusion due to insufficient energy input. During SLM, a local turbulent gas flow may be created by some byproducts, including low boiling point Zn vapor (907 °C [35]). The interaction of the laser and these byproducts would considerably impair the energy input. The laser source utilized in our SLM device is a Gaussian mode, which may further diminish the energy input at the edge of the laser spot. Therefore, irregular micropores were easily produced at the molten pool boundaries owing to a few unmelted particles.

Fig. 6b and e presents the microstructures and substructures of the SLM samples on the different cross-sections. As observed in Fig. 6b, only dense equiaxed grains containing fine cellular structures were detected on the XY cross-section. Contrastingly, a gradient structure composed of equiaxed grains and columnar dendrites (yellow arrows in Fig. 6e) was visualized within the molten pools, especially at the boundary regions. This unique structure was dominated under the synergic effect of the temperature gradient ($G$) and solidification velocity ($R$) of the molten pools during the SLM fabrication. However, it's quite difficult to distinguish the grain formation mechanism only via the SEM images. Hence, detailed analysis will be presented in EBSD part (Fig. 7).

The distribution of the main alloying elements is displayed in Fig. 6c, f, and Table 8. Intergranular structures are the Al-rich regions (i.e., micro regions 3 and 4) where abundant Al element was detected. Interestingly, except for the grain boundaries, intensity of Al element in α-Mg matrix was also high (Fig. 6c, f), indicating a large amount of Al dissolved in the matrix. The maximum solid solubility of Al in magnesium is as high as 12.9 wt% based on the Mg–Al phase diagram [36]. Thus, such high cooling rate of SLM ($10^4$–$10^6$ K/s [15,16]) would cause a large amount of Al element to dissolve into the α-Mg matrix, and cannot produce the coarse reticular β-$Al_{12}Mg_{17}$ structures like the cast state (Fig. 5). Existence of a small amount of fine and dense Al-rich regions also proves that the content of β-$Mg_{17}Al_{12}$ phase in the SLM samples is much lower than that of the cast samples, which was also observed from XRD analysis.

Fig. 7 presents the EBSD results of the SLM samples under different cross-sections to explore the grain growth mechanism and crystallographic orientation. As displayed in Fig. 7a, an inverse pole figure (IPF) of XY cross-section, average width of the laser tracks (white dash lines) was 24.12 ± 0.025 μm much less than that of the laser spot size (i.e., 45 ± 4 μm). Under irradiation of the high-intensity laser, low melting point Mg-based powder would be easily fused, thus a series of narrow laser tracks with high overlap ratio are produced. Microstructure of the XY cross-sections was mainly composed of a large quantity of ultra-fine equiaxed grains. Only a bit of coarse grain regions (black arrow) formed near the boundaries due to the intrinsic heat treatment (IHT) during SLM. As detected in Fig. 7b, average grain size of the XY cross-section is 1.95 ± 0.125 μm. Particularly, submicron grains (<1 μm: 18.14%) and ultrafine grains (1–2 μm: 38.78%) occupy a large fraction, exerting a substantial effect on the mechanical properties. The pole figures (PFs) in Fig. 7c do not present a symmetrical tendency, although the HCP structure has a good symmetry. The maximum multiple of uniform density (MUD) in {0001} PF is merely 1.44 («5), indicating a random texture on the XY cross-section. Notably, the strongest MUD can be grasped near the Z axis of the {0001} PF (i.e., building direction),

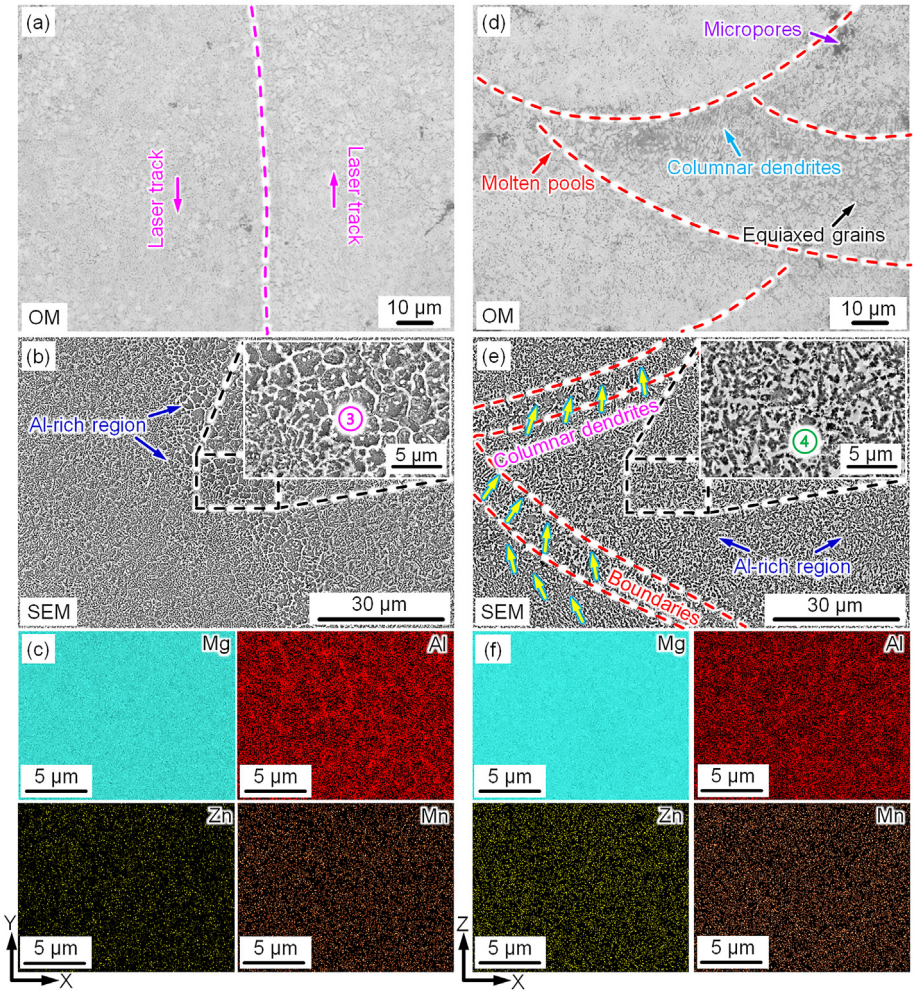


**Fig. 6.** Microstructure features of the SLM Mg–9Al–1Zn–0.5Mn samples on XY cross-section: (a) OM; (b) SEM; (c) main elements distribution of magnified view of (b); and on XZ cross-section: (d) OM; (e) SEM; (f) main elements distribution of magnified view of (e).

demonstrating a texture tendency along the building direction. Lack of dominant texture in PFs can be attributed to the non-uniform G in the molten pools caused by the in-situ formation of nanoparticles (like β-$Al_{12}Mg_{17}$) as well as the 67° rotation scanning strategy, leading to the absence of a preferred direction of solidification.

IPF of the SLM sample on the XZ cross-section is displayed in Fig. 7d. The gradient structures constituted with quite fine columnar dendrites and equiaxed grains can be observed. Formation and distribution of the columnar dendrites and equiaxed grains were not only governed by the ratio of *G/R*, but also affected by the heat dissipation direction and melt flow behavior [37]. During the rapid solidification, *G* between the molten pools and the low-temperature substrate is quite high along with a low *R* value, resulting in a high *G/R*. A typical characteristic of epitaxial columnar dendrites perpendicular to the molten pool interface was thus formed. Since the heat dissipation direction at the bottom of the molten pool was mainly through the surrounding solidified multi-tracks and powder bed, the growth direction of dendrites was mostly opposite to the heat dissipation direction (blue arrows in Fig. 7d). *G/R* value at the top of the molten pools was low due to a high *R* caused by the multiple convection heat transfer routes, i.e., from the center to the periphery of the molten pools, and from the surface of the molten pools to the surrounding environment. Moreover, heterogeneous nucleation would occur at the top of the molten pools, facilitated by the partially melted powders and some in-situ formed nanoparticles. Hence, large quantities of fine equiaxed grains were generated at the top of the molten pool. However, remelting phenomenon caused by the SLM process not only led to the fewer equiaxed grains on the XZ cross-section than the XY cross-section (Fig. 7a), but also the dendrite coarsening due to the IHT effect (black arrow in Fig. 7d). Interestingly, columnar dendrites would also grow obliquely in the direction of melt flow (indicated by pink arrows in Fig. 7d). The melt flow scoured the solute-rich layer at the front of the columnar dendrites, resulting in an uneven distribution of the solutes around the dendrite tips. Consequently, solute concentration towards the melt flow direction is lower than that away from the melt flow direction, further suppressing grain growth away from the direction of melt flow. Therefore, the grain growth direction would be biased towards the laser scanning direction (indicated by the pink and blue arrows in Fig. 7d).

As detected in Fig. 7e, average grain size on the XZ cross-section (3.11 ± 0.118 μm) is 59.49% coarser than that of the XY counterpart (1.95 ± 0.125 μm in Fig. 7b). Especially, appropriation of the submicron grains (<1 μm: 7.18%) and ultrafine grains (1–2 μm: 66.82%) is lower than that of the XY one. Notably, the maximum MUD is only 2.68 («5) presented in PFs (Fig. 7f), indicating a random texture, despite a large quantity of columnar dendrites generated within the XZ cross-section. Similar to the {0001} PF on the XY cross-section, the strongest texture is near the Z-axis. Hence, although a texture tendency along the building direction existed on the XZ cross-section, however, the whole SLM Mg–9Al–1Zn–0.5Mn sample was still dominated by the random texture.

Fig. 8 and Table 9 reveal the nanostructures and specific compositions of some micro-regions within the SLM samples characterized using TEM. Bright field image (BFI) was captured along the $[2\bar{1}\bar{1}0]$ axis (i.e., a-direction in the HCP system), which can be demonstrated by the selected

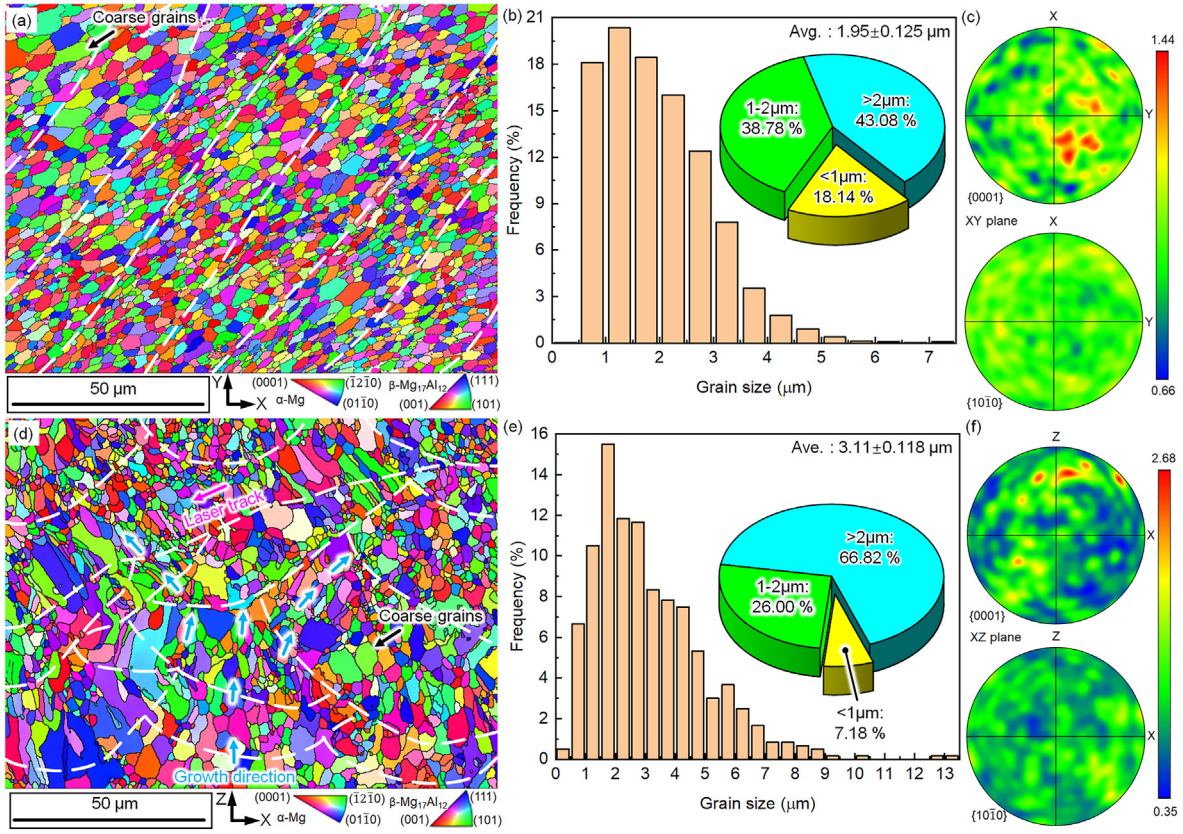


**Fig. 7.** EBSD results of the SLM Mg–9Al–1Zn–0.5Mn samples on XY cross-section: (a) IPF; (b) PFs; (c) grain size statistics; and on XZ cross-section: (d) IPF; (e) PFs; (f) grain size statistics.

**Table 8**
EDS analysis of elemental composition for different micro-regions in the SLM samples.

| Terms | Region 3 | | Region 4 | |
|---|---|---|---|---|
| | Weight (wt.%) | Atom (at.%) | Weight (wt.%) | Atom (at.%) |
| Mg | 81.62 | 83.65 | 82.56 | 84.26 |
| Al | 17.17 | 15.85 | 16.86 | 15.50 |
| Zn | 0.71 | 0.27 | 0.38 | 0.14 |
| Mn | 0.50 | 0.23 | 0.20 | 0.09 |

area electron diffraction (SAED) of the α-Mg matrix as displayed in Fig. 8a. Numerous nanoparticles evenly distributed in the fine equiaxed grains (1.58 ± 0.367 μm similar to the EBSD results) arouse plenty of dislocation walls (marked by blue arrow). As seen in Fig. 8b, large spherical nanoparticles (~95 nm) were pinned around the dislocation lines (pink arrows), resulting the dislocation tangles. With the help of SAED pattern and EDS results (micro region 5 in Table 9), these spherical nanoparticles can be confirmed as the β-$Al_{12}Mg_{17}$ phase. Interestingly, there are no parallel crystallographic planes between the α-Mg matrix and the β-$Al_{12}Mg_{17}$ particles despite $[2\bar{1}\bar{1}0]_\alpha$// $[111]_\beta$. Thus, it is reasonable to believe that these β-$Al_{12}Mg_{17}$ nanoparticles retained within the SLM samples were derived from some incompletely fused β-structures in the feedstocks, further leading to a dislocation strengthening.

Use of STEM enabled further visualization of nanoparticles and their morphology as seen in Fig. 9a. Combined with the distribution of main elements (Fig. 9b) and the atomic ratio of micro-region 6 (Mg:Al≈17:12 in Table 9), the long lathlike nanoparticles with a width of about 25 nm can be identified as β-$Al_{12}Mg_{17}$ phase. Different from the spherical β phase characterized in Fig. 8, the β phase in Fig. 9a has a Burgers orientation relationship with α-Mg matrix (i.e., $[2\bar{1}\bar{1}0]_\alpha$// $[1\bar{1}5]_\beta$ and $[\bar{1}011]_\alpha$// $[3\bar{2}\bar{1}]_\beta$), as shown in the SAED map of Fig. 9c. A large amount of dissolved Al element existed within the SLM samples due to the rapid solidification, as discussed in the SEM part. Therefore, numerous nano-β particles were precipitated under the IHT effect, further pinning the dislocation lines. Interestingly, quantities of short rod-like Mn-rich particles were also found around the subgrain boundaries in Fig. 9a and b. Ignoring the influence of Mg element within the matrix, combined with the EDS results of micro-region 7 (Al:Mn˜8:5 in Table 9) and the SAED pattern (Fig. 9c), the short rod-shaped nanoparticles can be determined as $Al_8Mn_5$ phase. According to the Mg–Al–Mn ternary phase diagram (Fig. 9d [38]), a series of metallurgical reactions would occur in the Mn-rich melt, as indicated by the pink red dot:

$$L \overset{950-1000^\circ C}{\rightarrow} \beta - Mn + L \overset{900-950^\circ C}{\rightarrow} Al_8Mn_5 + \alpha - Mg + L \quad (6)$$

$$Al_{11}Mn_4 + \alpha - Mg \overset{600-620^\circ C}{\rightarrow} Al_4Mn + Mg_{17}Al_{12} + \alpha - Mg \quad (7)$$

Nevertheless, owing to an extremely high cooling rate of the SLM, only high-temperature $Al_8Mn_5$ phase was formed and preserved instead of $Al_{11}Mn_4$ and $Al_4Mn$ phases. Notably, based on the planar lattice disregistry calculations [39], the lowest lattice mismatch of the $(0001)_{\alpha\text{-Mg}}$ and $(110)_{Al8Mn5}$ is 22.07% much higher than that of the $(111)_{\beta\text{-Mg17Al12}}$ and $(111)_{Al8Mn5}$ (1.21%). Hence, short rod-shaped $Al_8Mn_5$ nanoparticles can not only promote the nucleation and growth of the β phase (Fig. 9a), but also trigger a dispersion strengthening due to its incoherent interface with the matrix.

### 3.4. Mechanical properties and tensile behavior

Detailed mechanical properties of the Mg–9Al–1Zn–0.5Mn samples fabricated via different process are presented in Fig. 10 and Table 10. Average microhardness of the SLM samples (95.6 ± 5.28 $HV_{0.1}$) is about

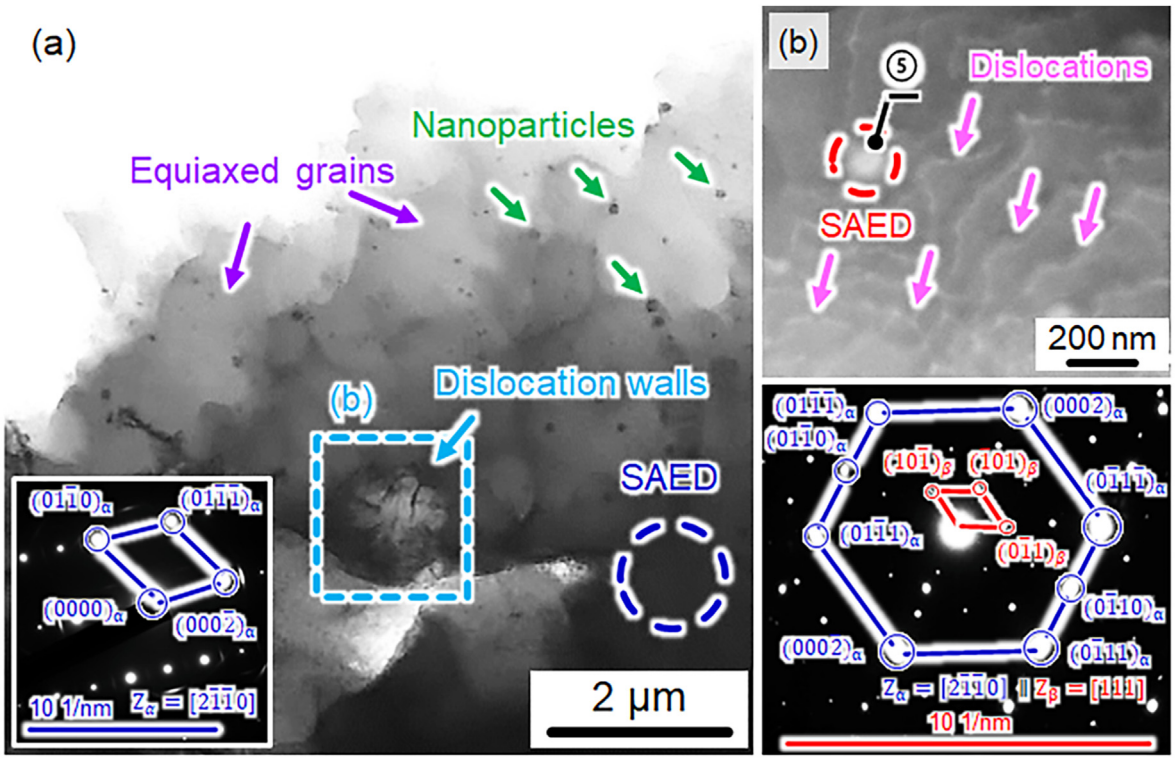


**Fig. 8.** TEM observations of the SLM Mg–9Al–1Zn–0.5Mn samples: (a) BFI; (b) magnified view of (a) under the HAADF mode and the corresponding SAED.

**Table 9**
EDS analyzing results of the different micro-regions within the TEM foils.

| Terms | Region 5 | | Region 6 | | Region 7 | |
|---|---|---|---|---|---|---|
| | Weight (wt.%) | Atom (at.%) | Weight (wt.%) | Atom (at.%) | Weight (wt.%) | Atom (at.%) |
| Mg | 60.66 | 63.12 | 54.64 | 57.21 | 47.68 | 58.00 |
| Al | 39.34 | 36.88 | 45.36 | 42.79 | 24.84 | 27.21 |
| Mn | / | / | / | / | 27.48 | 14.79 |
| Zn | / | / | / | / | / | / |

30.1% higher than that of the powders (73.3 ± 6.89 $HV_{0.1}$) and cast counterparts (74.0 ± 4.01 $HV_{0.1}$). Notably, all mechanical property indexes of the SLM samples are much better than those of the cast ones. Specifically, the UTS (370.2 MPa) and $A_t$ (10.4%) of the SLM specimens with the best mechanical properties are 145.5% and 300% higher than those of the cast sample (UTS = 150.8 MPa, $A_t$ = 2.5%), respectively. Favorable elastic modulus (39.8–42.4 GPa) of the SLM samples, close to that of the human cortical bone (10–30 GPa [40]), also shows an excellent prospect for bone implant applications.

A UTS-At bubble map of the biomedical magnesium alloys fabricated using different processes is depicted in Fig. 11. Normally, UTS of the magnesium alloys are quite difficult to surpass 300 MPa as well as maintaining a good ductility (i.e., $A_t$>5%) if without a series of post-treatment processes. However, the ultra-low grain size and nanoparticle strengthening observed in Mg–9Al–1Zn–0.5Mn SLM samples can enhance their mechanical properties. Thus, SLM-produced high-performance biomedical magnesium alloys offer sufficient data support and a theoretical basis for the customized medical implants.

Fig. 12 demonstrate the fractographies of the Mg–9Al–1Zn–0.5Mn samples under cast and SLM state, respectively. Generally, fracture mechanism of Mg-based materials at ambient temperature is brittle as cleavage or quasi-cleavage mode due to the few activated slip system within the HCP structures. As displayed in Fig. 12a, there is no necking phenomenon on the fracture surface of the cast samples. Notably, numerous micro cracks (pink arrows) and cleavage facets (green arrows) can be detected (Fig. 12a and b), indicating a typical cleavage fracture failure. As analyzed in the previous part (Fig. 5), micro cracks may be easily produced between the matrix (i.e., α-Mg phase) and high-hard intermetallics (i.e., β-$Al_{12}Mg_{17}$ structures) during the tensile test. Then, micro cracks would further propagate along the coarse grain boundaries, thus leading to a brittle fracture of the cast samples.

Unlike the cast state, a clear necking phenomenon (black arrows) can be observed within the SLM samples, as revealed in Fig. 12c. Moreover, a number of large dimples (oranges arrows) and tearing ridges (purple arrows) can be observed in Fig. 12d, presenting a ductile fracture feature. Nevertheless, a few residual powder particles still exist on the fracture surface, playing an adverse impact on the ductility. As such, significant improvements in mechanical properties were accompanied by a transition from a brittle fracture (Fig. 12a and b) for cast samples to a ductile fracture mode for SLM samples (Fig. 12c and d).

Based on the aforementioned characterization results, improvement in yield strength ($\sigma_{YS}$, MPa) of the SLM Mg–9Al–1Zn–0.5Mn samples can be principally attributed to grain boundary strengthening ($\sigma_{GB}$, MPa), solid solution strengthening ($\sigma_{SS}$, MPa) and precipitation hardening ($\sigma_P$, MPa). Thus, $\sigma_{YS}$ can be predicted through function (8):

$$\sigma_{YS} = \sigma_{GB} + \sigma_{SS} + \sigma_P \tag{8}$$

Strength increment associated with the grain size can be evaluated by the Hall-Petch formula as follows [49]:

$$\sigma_{GB} = \sigma_0 + kd^{-1/2} \tag{9}$$

where $\sigma_0$ = 11 MPa is the lattice intrinsic resistance to dislocation motion [49], $k$ = 164 MPa $\mu m^{1/2}$ is the constant for grain boundary strengthening contribution [50], and $d$ = 2.53 ± 0.181 μm is effective grain size obtained from EBSD statistics.

Effect of solid solution strengthening on the strength increment can be expressed as below [51]:

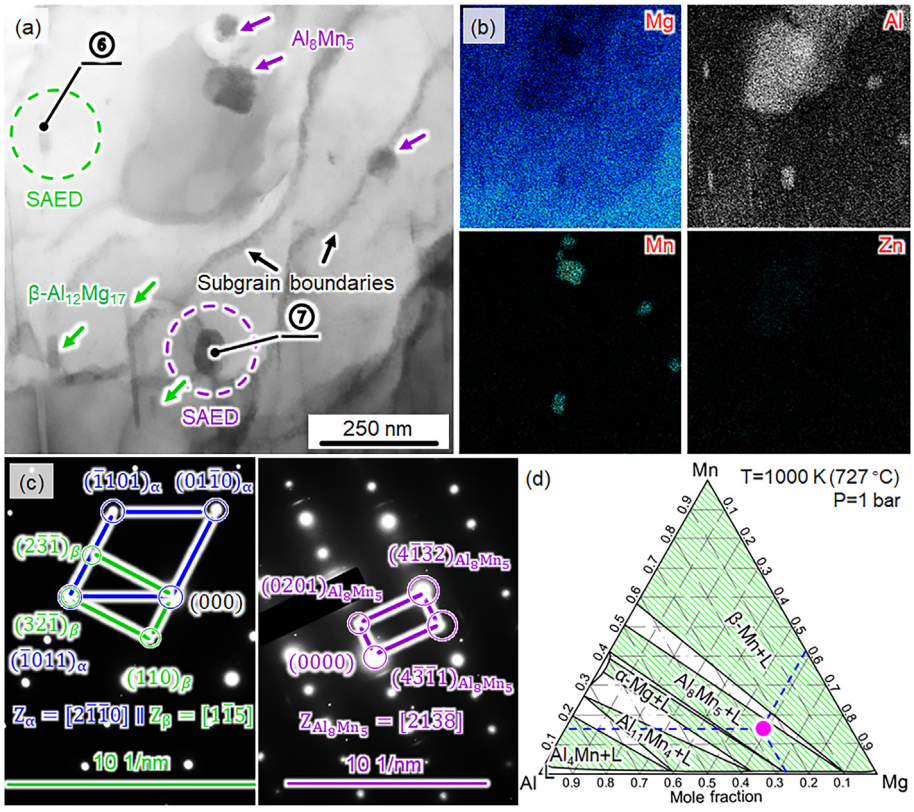


**Fig. 9.** STEM-EDS results of the SLM Mg–9Al–1Zn–0.5Mn samples: (a) BFI; (b) mapping; (c) SAED of the different micro-regions within (a); (d) cross-section of the Mg–Al–Mn ternary phase diagram (1000 K, 1 bar) [38].

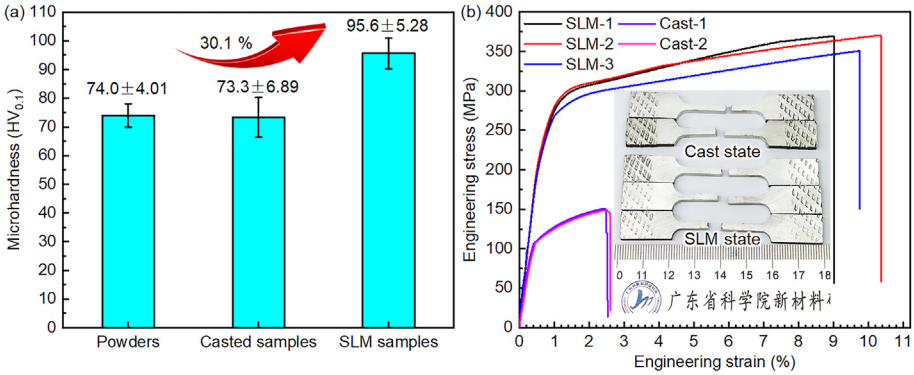


**Fig. 10.** (a) Microhardness distribution and (b) tensile strength of the Mg–9Al–1Zn–0.5Mn samples under different states.

**Table 10**
Mechanical properties of the Mg–9Al–1Zn–0.5Mn samples under different states.

| State | Microhardness ($HV_{0.1}$) | YS (MPa) | UTS (MPa) | E (GPa) | $A_t$ (%) |
|---|---|---|---|---|---|
| Powders | 74.0 ± 4.01 | / | / | / | / |
| Cast sample-1 | 76.4 ± 6.78 | 114.2 | 150.8 | 32.3 | 2.5 |
| Cast sample-2 | 70.2 ± 5.02 | 112.3 | 148.9 | 30.4 | 2.6 |
| SLM sample-1 | 95.2 ± 5.44 | 261.2 | 369.1 | 41.7 | 9.0 |
| SLM sample-2 | 94.8 ± 5.08 | 269.9 | 370.2 | 42.4 | 10.4 |
| SLM sample-3 | 96.7 ± 5.03 | 254.6 | 350.2 | 39.8 | 9.8 |

$$\sigma_{SS} = \sigma_u + \frac{3.1\varepsilon G c^{1/2}}{700} \quad (10)$$

where $\sigma_u$ = 39 MPa is yield strength of pure magnesium [52], $\epsilon$ = 0.74 MPa is an experimental parameter [53], $G = 1.66 \times 10^4$ MPa is the shear modulus of the matrix [54], and $c$ is the concentration of the solute (at.%). Only the solid solution strength effect of Al element was considered in this study but neglecting the effects of Zn and Mn elements due to the quite low of the Zn element (0.59 wt%) and Mn element (0.28 wt%) within the SLM samples. Thus, $c_{Al}$ can be determined as 6.57 ± 0.211 at.% after calculating according to the results of Tables 1 and 6.

Strength enhancement derived from the precipitation hardening was mainly triggered by the numerous β-$Mg_{17}Al_{12}$ nanoparticles, as characterized in Figs. 8 and 9. Owing to the different crystallographic structures and lattice constants between the high-hardness nanoparticles and matrix, thus, four main factors constitute the improvement caused by the

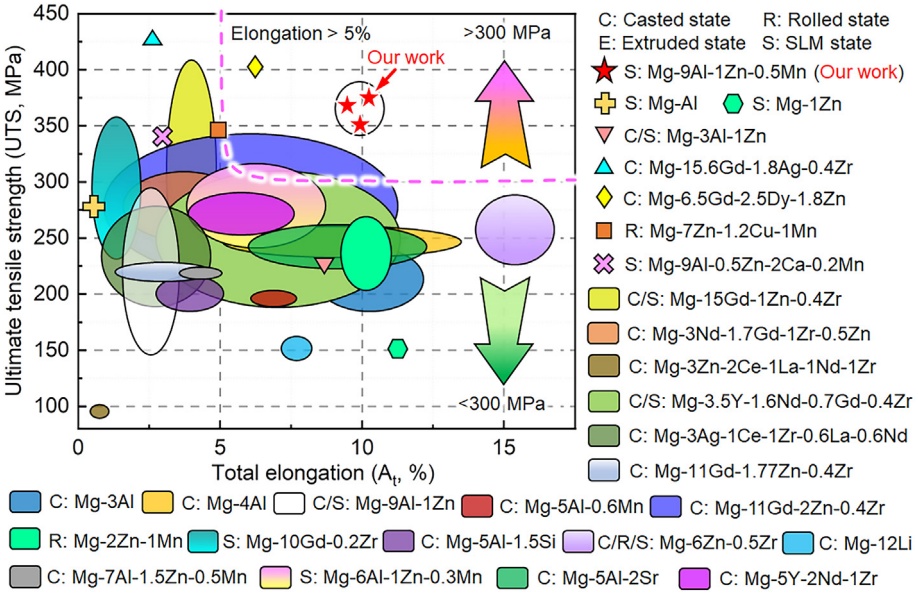


**Fig. 11.** UTS-A$_t$ bubble map of the biomedical magnesium alloys fabricated via different processes [1,5,9,10,15,20,22,26,27,41–48].

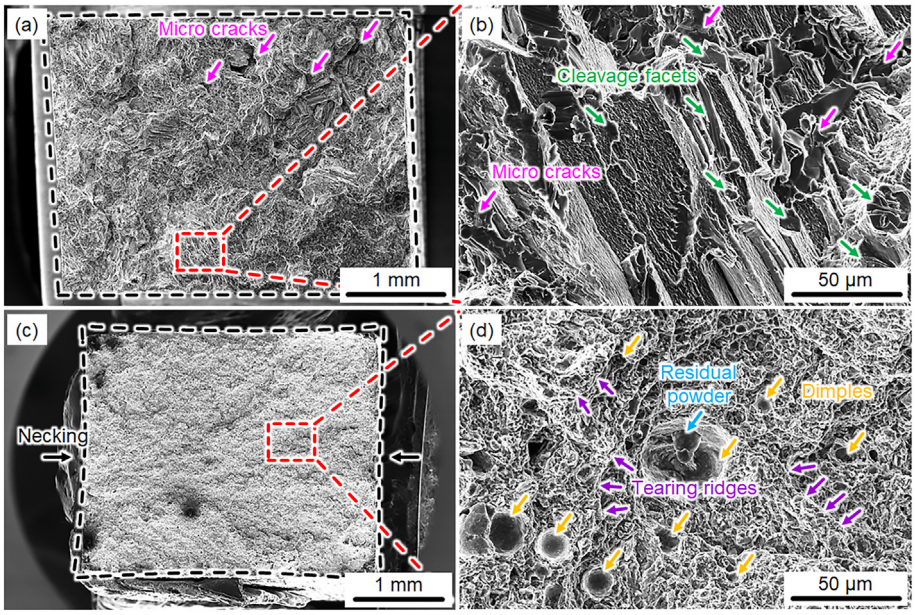


**Fig. 12.** Representative SEM fractography images of the Mg–9Al–1Zn–0.5Mn samples under: (a) cast state and (b) enlarged view of (a); (c) SLM state and (d) enlarged view of (c).

precipitation hardening mechanism, i.e., Orowan strengthening ($\sigma_{Orowan}$, MPa), load-bearing effect ($\sigma_{LB}$, MPa), coefficient of thermal expansion (CTE) mismatch ($\sigma_{CTE}$, MPa), and geometrically necessary dislocation density ($\sigma_{GND}$, MPa) [55]. Therefore, the $\sigma_P$ could be evaluated as follows:

$$\sigma_P = \sigma_{Orowan} + \sigma_{LB} + \sigma_{CTE} + \sigma_{GND} \tag{11}$$

The strength increment due to the Orowan process between the nanoparticles and the matrix ($\sigma_{Orowan}$, MPa) can be evaluated by the following formular [56]:

$$\sigma_{Orowan} = \frac{Gb}{2\pi\sqrt{1-\nu}\left[\left(\frac{0.779}{\sqrt{f}}\right) - 0.785\right]d_t} \ln\frac{0.785 d_t}{b} \tag{12}$$

where $b = 3.21 \times 10^{-10}$ m is the Burgers vector [54], $\nu = 0.35$ is the Poisson ratio [53], $d_t$ is the mean grain size of the reinforced

**Table 11**
Contributions of the different strengthening mechanisms for YS of the SLM Mg–9Al–1Zn–0.5Mn sample.

| Designations | | Strengthening contribution (MPa) | Fraction (%) |
|---|---|---|---|
| $\sigma_{GB}$ | | 114.11 | 38.11 |
| $\sigma_{SS}$ | | 52.94 | 17.68 |
| $\sigma_P$ | $\sigma_{Orowan}$ | 13.36 | 4.46 |
| | $\sigma_{LB}$ | 0.65 | 0.23 |
| | $\sigma_{CTE}$ | 62.40 | 20.84 |
| | $\sigma_{GND}$ | 55.93 | 18.68 |
| Predicted $\sigma_{YS}$ | | 299.40 | N/A |
| Experimental $\sigma_{YS}$ | | 269.90 | N/A |

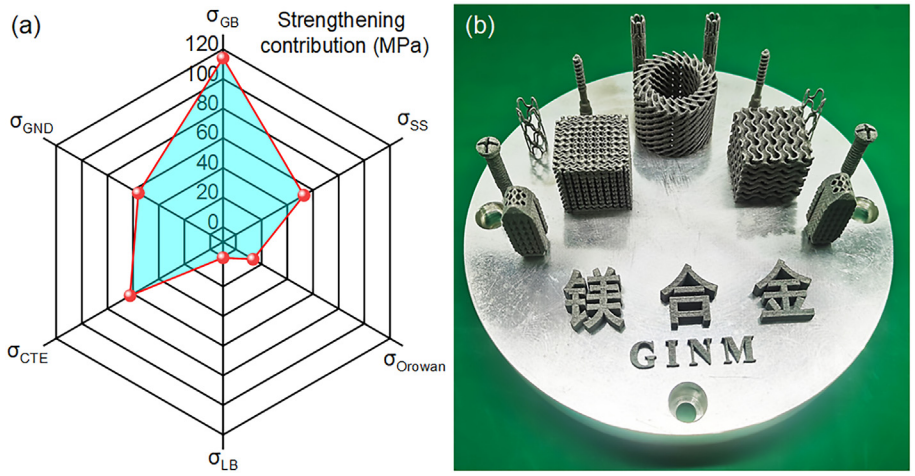


**Fig. 13.** (a) Strengthening mechanism-Contribution radar map of the SLM Mg–9Al–1Zn–0.5Mn sample; (b) SLM-fabricated different types of the biomedical implants.

nanoparticles, and $f$ is the fraction of these high-hardness nanoparticles. After measuring and calculating the above indicators in 10 TEM micrographs, $d_t$ and $f$ of this study can be confirmed as 84.86 ± 2.156 nm and 1.85 ± 0.118%, respectively.

Improvement induced by the load-bearing effect from the matrix to the enhanced nanoparticles ($\sigma_{LB}$, MPa) can be described as follows [55]:

$$\sigma_{LB} = 0.5\sigma_m f \tag{13}$$

where $\sigma_m$ = 70 MPa is YS of the Mg–Al alloy matrix [57].

$\sigma_{CTE}$ due to the difference between the thermal expansivities of the matrix and the nanoparticles can be described via the following function [56]:

$$\sigma_{CTE} = \alpha G b \left(\frac{12\Delta T \Delta C f}{b d_t}\right)^{1/2} \tag{14}$$

where $\alpha = 1.25$ is a constant [55], $\Delta T$ is the temperature increment (the processing temperature is 873 K and the ending temperature is 293 K) [58], $\Delta C$ ($\Delta C = C_{Mg} - C_{Mg17Al12}$) is the difference between the CTEs of the matrix and the nanoparticles ($C_{Mg} = 2.61 \times 10^{-5}\ K^{-1}$, $C_{Mg17Al12} = 7.5 \times 10^{-6}\ K^{-1}$ [57]).

Contribution of the geometrically necessary dislocation density ($\sigma_{GND}$, MPa) is presented below [55]:

$$\sigma_{GND} = \alpha G b \left(\frac{f 8\gamma}{b d_t}\right)^{1/2} \tag{15}$$

where $\gamma$ = 0.013 is the shear strain calculated using the Taylor factor [55].

By substituting Eqs. 12–15 into Eq. (11), we can attain the $\sigma_P$ due to the precipitation hardening. After calculating Eqs. (9) and (10), $\sigma_{GB}$ and $\sigma_{SS}$ can be obtained. Predicted results are demonstrated in Table 11 and Fig. 13a, indicating a good consistency with the experimental one (i.e., Predicted $\sigma_{YS}$ = 299.40 MPa, Experimental $\sigma_{YS}$ = 269.90 MPa). Contributions of various strengthening mechanisms to the YS is as follows: $\sigma_P > \sigma_{GB} > \sigma_{SS}$. Hence, precipitation hardening can be regarded as the dominant factor in the strengthening mechanism of the SLM Mg–9Al–1Zn–0.5Mn samples. Fig. 13b exhibits a variety of SLM biomedical implants fabricated using the optimized parameters, demonstrating the infinite possibilities of SLM Mg-based materials in the biomedical applications.

## 4. Conclusions

Mg–9Al–1Zn–0.5Mn specimens with ultra-high tensile strength and excellent ductility was directly manufactured via SLM process. Microstructural evolution, phase transformation, crystallographic texture, and mechanical properties of SLM Mg–9Al–1Zn–0.5Mn samples were systematically studied in this work. The primary conclusions are listed as follows:

(1) Mg–9Al–1Zn–0.5Mn samples with high relative density (99.5 ± 0.28%), good microhardness (95.6 ± 5.28 $HV_{0.1}$), outstanding strength (UTS = 370.2 MPa), and favorable ductility ($A_t$ = 10.4%) were fabricated using the optimized SLM processing parameters (i.e., $P$ = 120 W, $v$ = 500 mm/s, and $h$ = 45 μm).
(2) α-Mg phase (JCPDS # 35–0821) and β-$Al_{12}Mg_{17}$ phase (JCPDS # 73–1148) were detected within the SLM samples. These SLM samples are composed of ultra-fine equiaxed grains (Ave. grain size = 1.95 ± 0.125 μm) on the XY cross-sections and a gradient microstructure (Ave. grain size = 3.11 ± 0.118 μm) on the XZ cross-sections. The SLM Mg–9Al–1Zn–0.5Mn samples were dominated by the random texture.
(3) Numerous spherical β-$Al_{12}Mg_{17}$ ($[2\bar{1}\bar{1}0]_\alpha$// $[111]_\beta$), long lath-like β-$Al_{12}Mg_{17}$ ($[2\bar{1}\bar{1}0]_\alpha$// $[1\bar{1}5]_\beta$ and $[\bar{1}011]_\alpha$// $[3\bar{2}\bar{1}]_\beta$), and short rod-shaped $Al_8Mn_5$ nanoparticles were formed in the SLM samples.
(4) Contributions of the strengthening mechanisms to the yield strength is as follows: $\sigma_P > \sigma_{GB} > \sigma_{SS}$. Precipitation hardening can be considered as a principal element of the strengthening mechanism of the SLM Mg–9Al–1Zn–0.5Mn samples.

## Declaration of competing interest

The authors declare that they have no known competing financial interests or personal relationships that could have appeared to influence the work reported in this paper.

## Acknowledgements

This work was supported by the Sciences Platform Environment and Capacity Building Projects of GDAS (2021GDASYL-20210102005), the Guangdong Basic and Applied Basic Research Fund (2020A1515111031, 2021A1515010939), the Young Elite Scientist Sponsorship Program by China Association for Science and Technology (CAST) (YESS20210269), Guangdong Provincial Special Support Program (2019BT02C629), Guangdong Academy of Sciences Development Special Fund Project (2022GDASZH-2022010107), Guangdong Academy of Sciences International Science and Technology Cooperation Platform Construction Project (2022GDASZH-2022010203-003), Guangzhou Key Field R&D Program (20200702008).

## References


[1] Q. Deng, Y. Wu, Q. Wu, Y. Xue, Y. Zhang, L. Peng, W. Ding, Microstructure evolution and mechanical properties of a high-strength Mg–10Gd–3Y–1Zn–0.4Zr alloy fabricated by laser powder bed fusion, Addit. Manuf. 49 (2022), 102517, https://doi.org/10.1016/j.addma.2021.102517.

[2] Y. Yang, C. Lu, L. Shen, Z. Zhao, S. Peng, C. Shuai, In-situ deposition of apatite layer to protect Mg-based composite fabricated via laser additive manufacturing, J. Magnes. Alloy (2021), https://doi.org/10.1016/j.jma.2021.04.009.

[3] Y. Zheng, T. Zhang, Q. Wei, D. Fan, X. Liu, W. Li, C. Song, Y. Tian, H. Cai, Z. Liu, Improved osseointegration with rhBMP-2 intraoperatively loaded in a specifically designed 3D-printed porous Ti6Al4V vertebral implant, Biomater. Sci. 8 (2020) 1279–1289, https://doi.org/10.1039/c9bm01655d.

[4] J. Liang, Z. Lei, Y. Chen, W. Fu, X. Chen, S. Ma, Elimination of extraordinarily high cracking susceptibility of ZK60 Mg alloy fabricated by laser powder bed fusion, Mater. Lett. 312 (2022), 131731, https://doi.org/10.1016/j.matlet.2022.131731.

[5] K. Wei, M. Gao, Z. Wang, X. Zeng, Effect of energy input on formability, microstructure and mechanical properties of selective laser melted AZ91D magnesium alloy, Mater. Sci. Eng. 611 (2014) 212–222, https://doi.org/10.1016/j.msea.2014.05.092.

[6] B. Zhang, H. Liao, C. Coddet, Effects of processing parameters on properties of selective laser melting Mg-9%Al powder mixture, Mater. Des. 34 (2012) 753–758, https://doi.org/10.1016/j.matdes.2011.06.061.

[7] X. Niu, H. Shen, G. Xu, L. Zhang, J. Fu, X. Deng, Effect of aluminium content and processing parameters on the microstructure and mechanical properties of laser powder-bed fused magnesium-aluminium (0, 3, 6, 9wt%) powder mixture, Rapid Prototyp. J. 25 (2019) 744–751, https://doi.org/10.1108/RPJ-08-2018-0213.

[8] H. Somekawa, A. Kinoshita, A. Kato, Effect of alloying elements on room temperature stretch formability in Mg alloys, Mater. Sci. Eng. 732 (2018) 21–28, https://doi.org/10.1016/j.msea.2018.06.098.

[9] N.D., Granta Design, The CES EduPack 2022, 2022 http://www.grantadesign.com/education/eco/.

[10] K. Wei, X. Zeng, Z. Wang, J. Deng, M. Liu, G. Huang, X. Yuan, Selective laser melting of Mg–Zn binary alloys: Effects of Zn content on densification behavior, microstructure, and mechanical property, Mater. Sci. Eng. 756 (2019) 226–236, https://doi.org/10.1016/j.msea.2019.04.067.

[11] C. Chang, X. Yan, Z. Deng, B. Lu, R. Bolot, J. Gardan, S. Deng, M. Chemkhi, M. Liu, H. Liao, Heat treatment induced microstructural evolution, oxidation behavior and tribological properties of Fe–12Cr–9Ni–2Al steel (CX steel) prepared using selective laser melting, Surf. Coating. Technol. 429 (2022), 127982, https://doi.org/10.1016/j.surfcoat.2021.127982.

[12] D. Dong, C. Chang, H. Wang, X. Yan, W. Ma, M. Liu, S. Deng, J. Gardan, R. Bolot, H. Liao, Selective laser melting (SLM) of CX stainless steel: Theoretical calculation, process optimization and strengthening mechanism, J. Mater. Sci. Technol. 73 (2020) 151–164, https://doi.org/10.1016/j.jmst.2020.09.031.

[13] K. Wei, Z. Wang, X. Zeng, Influence of element vaporization on formability, composition, microstructure, and mechanical performance of the selective laser melted Mg–Zn–Zr components, Mater. Lett. 156 (2015) 187–190, https://doi.org/10.1016/j.matlet.2015.05.074.

[14] A. Iveković, N. Omidvari, B. Vrancken, K. Lietaert, L. Thijs, K. Vanmeensel, J. Vleugels, J.P. Kruth, Selective laser melting of tungsten and tungsten alloys, Int. J. Refract. Met. Hard Mater. 72 (2018) 27–32, https://doi.org/10.1016/j.ijrmhm.2017.12.005.

[15] Q. Deng, Y. Wu, Y. Luo, N. Su, X. Xue, Z. Chang, Q. Wu, Y. Xue, L. Peng, Fabrication of high-strength Mg–Gd–Zn–Zr alloy via selective laser melting, Mater. Char. 165 (2020), 110377, https://doi.org/10.1016/j.matchar.2020.110377.

[16] X. Yan, C. Chen, C. Chang, D. Dong, R. Zhao, R. Jenkins, J. Wang, Z. Ren, M. Liu, H. Liao, R. Lupoi, Study of the microstructure and mechanical performance of C-X stainless steel processed by selective laser melting (SLM), Mater. Sci. Eng. 781 (2020), 139227, https://doi.org/10.1016/j.msea.2020.139227.

[17] X.Y. Yao, J.C. Tang, Y.H. Zhou, Z.Z. Huang, J.B. Xu, Y. Long, L.L. Tan, B. Wiese, T. Ebel, M. Yan, Selective laser melting of an Mg/Metallic Glass hybrid for significantly improving chemical and mechanical performances, Appl. Surf. Sci. 580 (2022) 1–14, https://doi.org/10.1016/j.apsusc.2021.152229.

[18] C. Chang, S. Yue, W. Li, L. Lu, X. Yan, Study on microstructure and tribological behavior of the selective laser melted MgZnCa alloy, Mater. Lett. 309 (2022), 131439, https://doi.org/10.1016/j.matlet.2021.131439.

[19] X. Yao, J. Tang, Y. Zhou, A. Atrens, M.S. Dargusch, B. Wiese, T. Ebel, M. Yan, Surface modification of biomedical Mg–Ca and Mg–Zn–Ca alloys using selective laser melting : Corrosion behaviour , microhardness and biocompatibility, J. Magnes. Alloy 9 (6) (2020) 2155–2168, https://doi.org/10.1016/j.jma.2020.08.011.

[20] J. Liang, Z. Lei, Y. Chen, W. Fu, S. Wu, X. Chen, Y. Yang, Microstructure evolution of laser powder bed fusion ZK60 Mg alloy after different heat treatment, J. Alloys Compd. 898 (2022), 163046, https://doi.org/10.1016/j.jallcom.2021.163046.

[21] S. Liu, H. Guo, Balling behavior of selective laser melting (SLM) magnesium alloy, Materials 13 (16) (2020) 3632, https://doi.org/10.3390/MA13163632.

[22] H. Hyer, L. Zhou, Q. Liu, D. Wu, S. Song, Y. Bai, B. McWilliams, K. Cho, Y. Sohn, High strength WE43 microlattice structures additively manufactured by laser powder bed fusion, Materialia 16 (2021), 101067, https://doi.org/10.1016/j.mtla.2021.101067.

[23] J. Song, H. Zhao, J. Liao, B. Jiang, A. Zhang, Y. Huang, K.U. Kainer, N. Hort, F. Pan, Comparison on hot tearing behavior of binary Mg–Al, Mg–Y, Mg–Gd, Mg–Zn, and Mg–Ca alloys, Metall. Mater. Trans. A 53 (8) (2022) 2986–3001, https://doi.org/10.1007/s11661-022-06719-w.

[24] C. Gao, S. Li, L. Liu, S. Bin, Y. Yang, S. Peng, C. Shuai, Dual alloying improves the corrosion resistance of biodegradable Mg alloys prepared by selective laser melting, J. Magnes. Alloy. 9 (2021) 305–316, https://doi.org/10.1016/j.jma.2020.03.016.

[25] C. Shuai, C. He, P. Feng, W. Guo, C. Gao, P. Wu, Y. Yang, S. Bin, Biodegradation mechanisms of selective laser-melted Mg–xAl–Zn alloy: Grain size and intermetallic phase, Virtual Phys. Prototyp. 13 (2018) 59–69, https://doi.org/10.1080/17452759.2017.1408918.

[26] X. Niu, H. Shen, J. Fu, Microstructure and mechanical properties of selective laser melted Mg-9 wt% Al powder mixture, Mater. Lett. 221 (2018) 4–7, https://doi.org/10.1016/j.matlet.2018.03.068.

[27] X. Niu, H. Shen, J. Fu, J. Feng, Effective control of microstructure evolution in AZ91D magnesium alloy by SiC nanoparticles in laser powder-bed fusion, Mater. Des. 206 (2021), 109787, https://doi.org/10.1016/j.matdes.2021.109787.

[28] S.J.S. Chelladurai, K. Murugan, A.P. Ray, M. Upadhyaya, V. Narasimharaj, S. Gnanasekaran, Optimization of process parameters using response surface methodology: A review, Mater. Today Proc. 37 (2020) 1301–1304, https://doi.org/10.1016/j.matpr.2020.06.466.

[29] X. Yan, C. Chen, C. Chang, D. Dong, R. Zhao, R. Jenkins, J. Wang, Z. Ren, M. Liu, H. Liao, R. Lupoi, S. Yin, Study of the microstructure and mechanical performance of C-X stainless steel processed by selective laser melting (SLM), Mater. Sci. Eng. 781 (2020), 139227, https://doi.org/10.1016/j.msea.2020.139227.

[30] L. Alexander, H.P. Klue, Basic aspects of x-ray absorption in quantitative diffraction analysis of powder mixtures, Powder Diffr. 4 (1989) 66–69, https://doi.org/10.1017/S0885715600016432.

[31] C. Si, X. Tang, X. Zhang, J. Wang, W. Wu, Characteristics of 7055Al alloy powders manufactured by gas-solid two-phase atomization: A comparison with gas atomization process, Mater. Des. 118 (2017) 66–74, https://doi.org/10.1016/j.matdes.2017.01.028.

[32] M. Deutges, H.P. Barth, Y. Chen, C. Borchers, R. Kirchheim, Hydrogen diffusivities as a measure of relative dislocation densities in palladium and increase of the density by plastic deformation in the presence of dissolved hydrogen, Acta Mater. 82 (2015) 266–274, https://doi.org/10.1016/j.actamat.2014.09.013.

[33] H. Shahmir, T.G. Langdon, An evaluation of the hexagonal close-packed to face-centered cubic phase transformation in a Ti–6Al–4V alloy during high-pressure torsion, Mater. Sci. Eng. 704 (2017) 212–217, https://doi.org/10.1016/j.msea.2017.07.099.

[34] S.R.E. Williamson G K III., Dislocation densities in some annealed and cold-worked metals from measurements on the x-ray debye-scherrer spectrum, Philos. Mag. A 1 (1956) 34–36.

[35] J. Yi, C. Chang, X. Yan, Y. Xie, Y. Liu, M. Liu, K. Zhou, A novel hierarchical manufacturing method of the selective laser melted Al 7075 alloy, Mater. Char. 191 (2022), 112124, https://doi.org/10.2139/ssrn.4098746.

[36] A.H. Feng, Z.Y. Ma, Enhanced mechanical properties of Mg–Al–Zn cast alloy via friction stir processing, Scripta Mater. 56 (2007) 397–400, https://doi.org/10.1016/j.scriptamat.2006.10.035.

[37] X. Yan, S. Gao, C. Chang, J. Huang, K. Khanlari, D. Dong, W. Ma, N. Feneneche, H. Liao, M. Liu, Effect of building directions on the surface roughness , microstructure , and tribological properties of selective laser melted Inconel 625, J. Mater. Process. Technol. 288 (2021), 116878, https://doi.org/10.1016/j.jmatprotec.2020.116878.

[38] FactSage Datebase Documentation. https://www.factsage.com, 2021.

[39] F. Pan, Z. Feng, X. Zhang, A. Tang, The types and distribution characterization of Al–Mn phases in the AZ61 magnesium alloy, Procedia Eng. 27 (2012) 833–839, https://doi.org/10.1016/j.proeng.2011.12.528.

[40] K. Miura, N. Yamada, S. Hanada, T.K. Jung, E. Itoi, The bone tissue compatibility of a new Ti–Nb–Sn alloy with a low Young's modulus, Acta Biomater. 7 (2011) 2320–2326, https://doi.org/10.1016/j.actbio.2011.02.008.

[41] P. Fu, N. Wang, H. Liao, W. Xu, L. Peng, J. Chen, G. Hu, W. Ding, Microstructure and mechanical properties of high strength Mg−15Gd−1Zn−0.4Zr alloy additive-manufactured by selective laser melting process, Trans. Nonferrous Metals Soc. China 31 (2021) 1969–1978, https://doi.org/10.1016/S1003-6326(21)65630-3.

[42] J. Liang, Z. Lei, Y. Chen, S. Wu, X. Chen, M. Jiang, S. Cao, Formability, microstructure, and thermal crack characteristics of selective laser melting of ZK60 magnesium alloy, Mater. Sci. Eng. 839 (2022), 142858, https://doi.org/10.1016/j.msea.2022.142858.

[43] S. Julmi, A. Abel, N. Gerdes, C. Hoff, J. Hermsdorf, L. Overmeyer, C. Klose, H.J. Maier, Development of a laser powder bed fusion process tailored for the additive manufacturing of high-quality components made of the commercial magnesium alloy WE43, Materials 14 (2021) 1–19, https://doi.org/10.3390/ma14040887.

[44] R.E. Hendea, D. Raducanu, A. Nocivin, S. Ivanescu, D. Stanciu, C. Trisca-Rusu, R.S. Campian, S.I. Drob, V.D. Cojocaru, B.M. Gălbinașu, Laser powder bed fusion applied to a new biodegradable Mg–Zn–Zr–Ca alloy, Materials 15 (7) (2022) 2561, https://doi.org/10.3390/ma15072561.

[45] S. Liu, H. Guo, Influence of hot isostatic pressing (HIP) on mechanical properties of magnesium alloy produced by selective laser melting (SLM), Mater. Lett. 265 (2020), 127463, https://doi.org/10.1016/j.matlet.2020.127463.

[46] A. Pawlak, P.E. Szymczyk, T. Kurzynowski, E. Chlebus, Selective laser melting of magnesium AZ31B alloy powder, Rapid Prototyp. J. 26 (2020) 249–258, https://doi.org/10.1108/RPJ-05-2019-0137.

[47] Q. Deng, Y. Wu, N. Su, Z. Chang, J. Chen, L. Peng, W. Ding, Influence of friction stir processing and aging heat treatment on microstructure and mechanical properties of selective laser melted Mg–Gd–Zr alloy, Addit. Manuf. 44 (2021), 102036, https://doi.org/10.1016/j.addma.2021.102036.

[48] Q. Deng, Y. Wu, W. Zhu, K. Chen, D. Liu, L. Peng, W. Ding, Effect of heat treatment on microstructure evolution and mechanical properties of selective laser melted

Mg–11Gd–2Zn–0.4Zr alloy, Mater. Sci. Eng. 829 (2022), 142139, https://doi.org/10.1016/j.msea.2021.142139.
[49] L. Gao, R.S. Chen, E.H. Han, Microstructure and strengthening mechanisms of a cast Mg–1.48Gd–1.13Y–0.16Zr (at.%) alloy, J. Mater. Sci. 44 (2009) 4443–4454, https://doi.org/10.1007/s10853-009-3672-8.
[50] S.M. He, X.Q. Zeng, L.M. Peng, X. Gao, J.F. Nie, W.J. Ding, Microstructure and strengthening mechanism of high strength Mg–10Gd–2Y–0.5Zr alloy, J. Alloys Compd. 427 (2007) 316–323, https://doi.org/10.1016/j.jallcom.2006.03.015.
[51] R.W. Hertzberg, R.P. Vinci, J.L. Hertzberg, Deformation and Fracture Mechanics of Engineering Materials, third ed., Wiley publication, 1989.
[52] C.H. Cáceres, D.M. Rovera, Solid solution strengthening in concentrated Mg–Al alloys, J. Light Met. 1 (2001) 151–156, https://doi.org/10.1016/S1471-5317(01)00008-6.
[53] Z. Yang, J.P. Li, Y.C. Guo, T. Liu, F. Xia, Z.W. Zeng, M.X. Liang, Precipitation process and effect on mechanical properties of Mg–9Gd–3Y–0.6Zn–0.5Zr alloy, Mater. Sci. Eng. 454–455 (2007) 274–280, https://doi.org/10.1016/j.msea.2006.11.047.
[54] H.J. Frost, M.F. Ashby, Deformation-mechanism Maps: The Plasticity and Creep of Metals and Ceramics, Pergamon Press, New York, 1982.
[55] J.W. Luster, M. Thumann, R. Baumann, Mechanical properties of aluminium alloy 6061–Al2O3 composites, Mater. Sci. Technol. 9 (1993), 863–862.
[56] R.M. Aikin, L. Christodoulou, The role of equiaxed particles on the yield stress of composites, Scripta Metall. Mater. 25 (1991) 9–14, https://doi.org/10.1016/0956-716X(91)90345-2.
[57] M. Mabuchi, K. Higashi, Strengthening mechanisms of Mg–Si alloys, Acta Mater. 44 (1996) 4611–4618, https://doi.org/10.1016/1359-6454(96)00072-9.
[58] M.M. Avedesian, H. Baker, ASM Specialty Handbook Magnesium and Magnesium Alloys, ASM international, 1999.

**Cheng Chang** is a R & D Engineer in Prof. Min Liu and Prof. Kesong Zhou group of the Institute of New Materials, Guangdong Academy of Sciences. He received Ph.D. degree from University of Technology of Troyes (UTT, France) in 2021. Dr Chang's research interests focus on material design, process development and post-processing of high-performance alloys manufactured by selective laser melting (SLM).

**Xingchen Yan** is an associate professor in Prof. Min Liu and Prof. Kesong Zhou group of the Institute of New Materials, Guangdong Academy of Sciences. He received Ph.D. degree from University of Technology of Belfort- Montbéliard (UTBM, France) in 2018. His current research interests are focused on the design of advanced biomedical metal materials, analysis of the selective laser melted (SLM) high-performance metal matrix composites (MMCs).

**Min Liu** is a professorate senior engineer, doctoral supervisor, chief scientist of the National Basic Research Program of China (973 Program). He received his bachelor's degree from Central South University (1985) and master's degree from Institute of Metals, Chinese Academy of Sciences (1990). His research interests include thermal spray, surface modification, physical metallurgy and mechanical behavior of alloys, and additive manufacturing (3D printing).